TTI inversion of marine CSEM data

Kristian Rymann Hansen, Martin Panzner, Daniil Shantsev, and Rune Mittet*
Electromagnetic Geoservices ASA, Trondheim, Norway

SUMMARY

We present a 3D inversion algorithm for marine CSEM data which takes the electrical anisotropy of steeply-dipping sedimentary rock formations into account. This anisotropy can have a significant impact on CSEM data, and we show that failure to take it into account may lead to imaging artifacts, which complicates the interpretation of the resistivity image. We apply our algorithm to both synthetic data and a field data set acquired over the Perdido fold belt in the Gulf of Mexico, and compare the results from VTI and TTI inversions.

INTRODUCTION

Marine controlled-source electromagnetic (CSEM) surveying applied to hydrocarbon exploration has matured greatly in the past decade, and as a result has been applied in increasingly complex geology (Kanhalangsy et al., 2011). In particular, it has been shown that electrical anisotropy has a significant effect on marine CSEM data (Lu and Xia, 2007) , and that failure to take it into account can lead to severe imaging artifacts (Mohamad et al., 2010; Newman et al., 2010). State-of-the-art 3D inversion algorithms, such as those presented in e.g. (Morten et al., 2010; Newman et al., 2010), assume that the conductivity tensor is horizontally isotropic, which is known as vertical transverse isotropy (VTI). This assumption works well provided that the anisotropic formations do not have significant dip. However, recent modeling studies (Davydycheva and Frenkel, 2013; Li and Dai, 2011) have shown that the effect of dipping anisotropy, known as tilted transverse isotropy (TTI), can have a significant impact on marine CSEM data, and cannot be accurately modeled under the VTI assumption. A pertinent question is therefore what effect TTI has on VTI inversion, and how to properly account for TTI in inversion.

In this paper, we present a 3D inversion algorithm for marine CSEM data that takes TTI fully into account. We first apply the algorithm to a simple synthetic model representing an anticline structure with steep dip angles, and then to a 3D CSEM data set acquired over the Perdido fold belt in the Gulf of Mexico.

THEORY

Forward modeling of TTI media

The forward problem in CSEM is governed by Maxwell's equations in the quasi-static limit

$$\nabla \times \mathbf{E} = -\mu_0 \frac{\partial \mathbf{H}}{\partial t}, \tag{1}$$

$$\nabla \times \mathbf{H} = \Sigma \mathbf{E} + \mathbf{J}, \tag{2}$$

where $\mathbf{E}$ and $\mathbf{H}$ are the electric and magnetic field vectors, respectively, $\mathbf{J}$ is the source current density, and Σ is the conductivity tensor of the medium. In the case of TTI, the conductivity tensor is diagonal in a coordinate system aligned with the beds, called the principal coordinates, and can be written as

$$\Sigma = \mathbf{R}^T \begin{pmatrix} \sigma_p & & \\ & \sigma_p & \\ & & \sigma_n \end{pmatrix} \mathbf{R}, \tag{3}$$

where $\mathbf{R}$ is a rotation matrix from the principal coordinates to coordinates aligned with the horizontal and vertical directions. The two principal components σ_p and σ_n are the conductivity parallel and normal to the beds, respectively. The rotation matrix $\mathbf{R}$ is given in terms of two Euler angles α and β as

$$\mathbf{R} = \begin{pmatrix} \cos\alpha\cos\beta & \sin\alpha\cos\beta & -\sin\beta \\ -\sin\alpha & \cos\alpha & 0 \\ \cos\alpha\sin\beta & \sin\alpha\sin\beta & \cos\beta \end{pmatrix}, \tag{4}$$

where α is the azimuth angle and β is the dip angle.

We solve the forward problem using a finite-difference time-domain (FDTD) scheme applied to equations (1) and (2) after transforming these from the real-world domain, in which displacement currents are negligible, to a fictitious domain in which conduction currents are negligible, in order to speed up the calculation (Maaø, 2007). The equations are discretized on a Lebedev grid, similarly as in Davydycheva et al. (2003).

TTI inversion

Our 3D TTI inversion is formulated as a non-linear least-squares problem, with a cost function defined as

$$E(\mathbf{m}) = E_d(\mathbf{m}) + \lambda E_m(\mathbf{m}), \tag{5}$$

where $\mathbf{m}$ is a vector of model parameters, consisting of the logarithm of the two conductivity components, σ_p and σ_n, as well as the two Euler angles α and β for each cell in the model. The data part of the cost function is given by

$$E_d(\mathbf{m}) = \left(\mathbf{d}^{obs} - \mathbf{d}^{syn}(\mathbf{m})\right)^\dagger \mathbf{W}_d^T \mathbf{W}_d \left(\mathbf{d}^{obs} - \mathbf{d}^{syn}(\mathbf{m})\right), \tag{6}$$

where $\mathbf{d}^{obs}$ is a vector of the measured complex field components, and $\mathbf{d}^{syn}$ is the corresponding predicted data from the model. $\mathbf{W}_d$ is a diagonal data weighting matrix containing the inverse of the standard deviation of each data point, and the weighting scheme used here is described by Morten et al. (2009). The regularization term penalizes non-smooth models and is given by

$$E_m(\mathbf{m}) = (\mathbf{m} - \mathbf{m}^{ap})^T \mathbf{W}_m^T \mathbf{W}_m (\mathbf{m} - \mathbf{m}^{ap}), \tag{7}$$

where $\mathbf{m}^{ap}$ is an a priori model, which here is identical to the initial model used in the inversion. The matrix $\mathbf{W}_m$ represents spatial first derivative operators with respect to the three orthogonal coordinate axes of the local principal coordinates,

with a greater weight on the directions parallel to the beds such that the model is smoothed predominantly in the bed-parallel directions. The parameter λ in equation (5) is an overall scaling of the regularization term, which is adjusted to provide an adequate trade-off between data fit and model smoothness. The cost function in equation (5) is minimized using the quasi-Newton method L-BFGS-B (Zhu et al., 1997).

RESULTS

Synthetic model

We first test our inversion on a simple synthetic 2D model representing a steeply dipping anticline structure (see Figure 1). This model consists of an isotropic background of 1 Ωm resistivity and an anisotropic layer representing an anticline structure. The layer has a normal resistivity $\rho_n = 4$ Ωm and a parallel resistivity $\rho_p = 1$ Ωm. The dip angle of the two sloping flanks of the structure is 20 deg and 40 deg, respectively. The water layer is 2000 m deep, and has a resistivity of 0.3 Ωm.

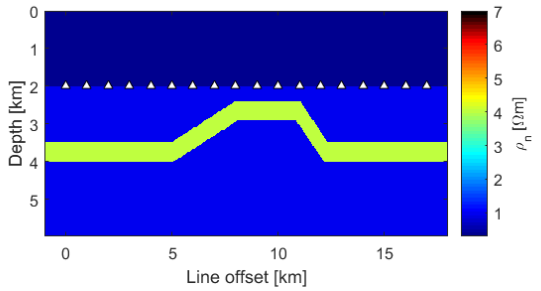

Figure 1: Normal resistivity ρ_n of the true model. White triangles indicate receiver positions along one of the towlines.

Synthetic data for this model was calculated using our TTI forward modeling code for a regular receiver grid consisting of 5 lines of 18 receivers each, spaced 1 km apart, and at frequencies of 0.1, 0.5, 1.0 and 1.5 Hz. The synthetic data was contaminated with 1% Gaussian multiplicative noise and additive noise with a standard deviation of 10^{-15} V/Am^2 for the horizontal electric field components.

The synthetic data was first inverted using a VTI inversion in which the Euler angles α and β were held fixed at 0 degrees. The initial model was a simple isotropic background model, which included only the conductivity of the sea and background formation. The inversion converged after 35 iterations, and the resulting model is shown in Figure 2. The vertical resistivity image, shown in Figure 2a, shows high-resistive artifacts on the slopes of the anticline structure, with the vertical resistivity component reaching nearly 8 Ωm. In addition, the slopes are imaged as high-resistive anomalies in the horizontal resistivity image (Figure 2b), because of the significant dip of the flanks of the structure, even though the parallel resistivity component of the layer in the true model is identical to the background. The VTI resistivity image may therefore be misinterpreted as representing hydrocarbon-charged stratigraphic traps on the flank of the anticline.

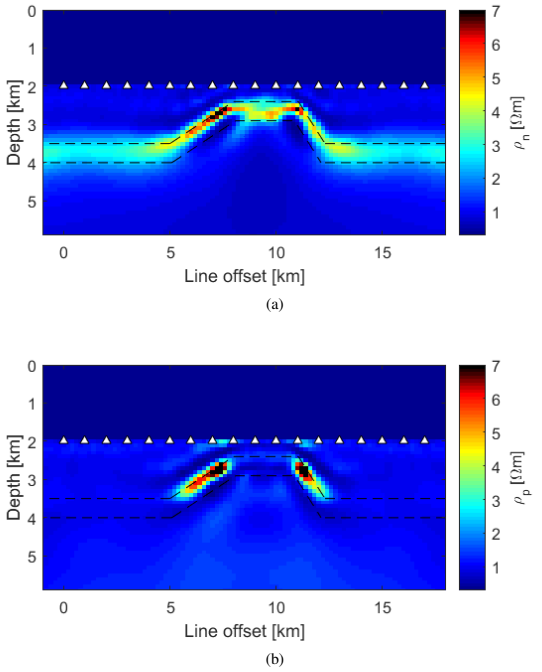

Figure 2: Vertical resistivity (a) and horizontal resistivity (b) for the VTI inversion of the synthetic model.

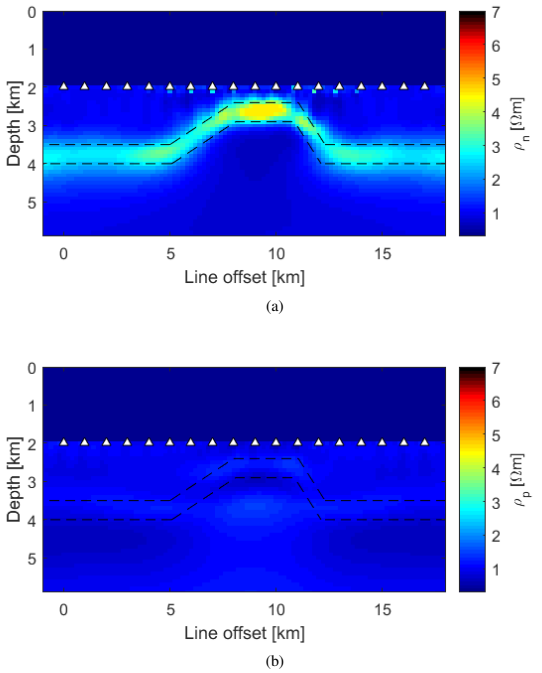

Figure 3: Normal resistivity (a) and parallel resistivity (b) for the TTI inversion of the synthetic model.

Next, we inverted the data using our TTI inversion, in which the inversion also updates the two Euler angles, using the same initial model as for the VTI inversion with both Euler angles set to zero. After 35 iterations, we obtained the resistivity image shown in Figure 3 and the dip angle β shown in Figure 4. The image is very consistent with the true model, not only in terms of the principal resistivity components but also the dip and azimuth angles, and does not have spurious anomalies on the flanks of the anticline. The fact that the flanks and deep parts of the resistive layer are imaged with a slightly too low resistivity is most likely due to reduced sensitivity to these parts of the model, compared to the shallow crest of the anticline.

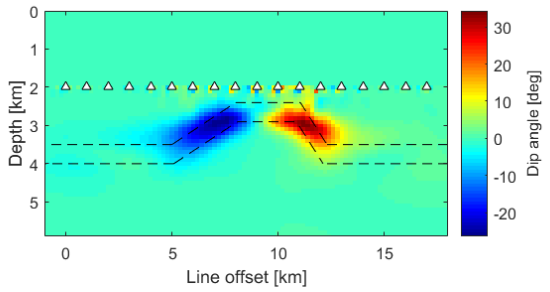

Figure 4: Dip angle for the TTI inversion of the synthetic model.

Field data

To test our TTI inversion on field data, we applied it to a 3D CSEM data set acquired over the Perdido fold belt in the Gulf of Mexico. The geology in this area consists of several steeply dipping anticline and syncline structures, and modeling such a geology using VTI modeling may therefore be inaccurate, possibly resulting in imaging artifacts. We first used our inversion as a VTI inversion, with all dip and azimuth angles fixed at zero degrees. The two horizontal electric field components E_x and E_y at frequencies of 0.125 Hz, 0.25 Hz, 0.5 Hz and 1 Hz were used as input data. The inversion converged to a RMS data fit of 1.6, and the resulting resistivity image is shown superimposed on a seismic section in Figure 5.

A first observation is that the subsurface is anisotropic, with a spatially varying anisotropy ratio around 3 in large portions of the model. We also see a localized high-resistive anomaly on the right flank of the anticline structure, visible only in the vertical resistivity component (label A in Figure 5a). Horizontal, thin resistive layers are typically only imaged in the vertical resistivity component, since the electric field is essentially vertical in such structures, and so the anomaly could be interpreted as a thin resistive layer associated with a hydrocarbon accumulation on the flank of the anticline structure. However, since the dip of the sediments in this part of the model is quite steep, on the order of $25-30$ degrees, we may suspect that this anomaly is an artifact caused by modeling the resistivity as VTI.

Another interesting feature is the presence of a weaker, more diffuse anomaly (label B in Figure 5a) located in the syncline to the left of the anticline structure in the vertical resistivity

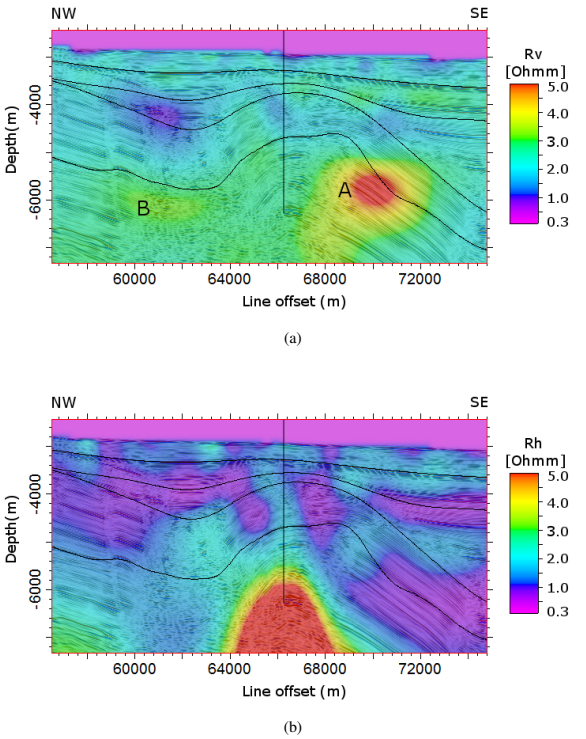

Figure 5: Vertical (a) and horizontal (b) resistivity components for the VTI inversion of the Perdido fold belt data.

model. Again, the steeply dipping sediments surrounding this anomaly lead us to suspect that it may be an imaging artifact. Finally, we note that the deep part of the model appears more resistive than the overlying sediments in the horizontal resistivity model (Figure 5b), while in the vertical model, no such difference is seen. This is most likely due to a lack of sensitivity to the vertical resistivity component in the deep part of the model.

Having performed the VTI inversion, we then applied the TTI inversion to the same data set. In this case, we produced an initial model with an initial guess for the azimuth and dip angles obtained by interpolating the slopes of a few horizons picked from the seismic. However, the inversion was still free to modify both angles. The TTI inversion converged to a RMS data fit of 1.3, slightly better than that of the VTI inversion, and produced the resistivity image shown in Figure 6.

While the image is broadly similar to the VTI inversion result, we note a number of interesting features. Firstly, the resistive anomaly seen on the right flank of the anticline structure in the VTI inversion is still present, and so is unlikely to be an inversion artifact caused by TTI effects. Secondly, the resistive anomaly in the syncline to the left of the anticline has vanished, indicating that its presence in the VTI inversion is likely an artifact caused by TTI effects. Instead the entire anticline structure has a higher normal resistivity component compared to the vertical resistivity component of the VTI inversion. Finally, the high-resistive deep part of the anticline is imaged as

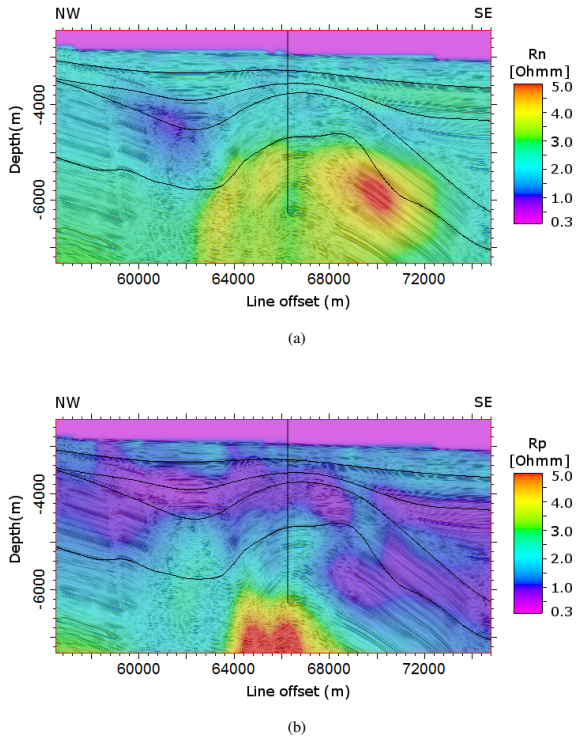

Figure 6: Normal (a) and parallel (b) resistivity components for the TTI inversion of the Perdido fold belt data.

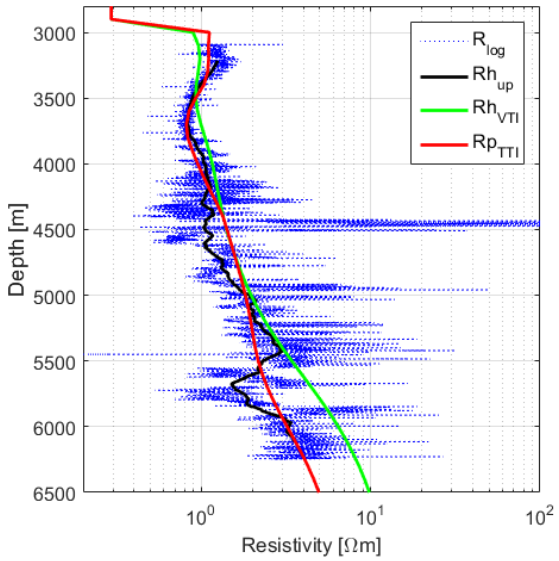

Figure 7: Comparison of upscaled well log resistivity to horizontal/parallel resistivity from the VTI and TTI inversions. The blue dots are the well log measurements, the black curve is the upscaled well log, the green curve is the VTI horizontal resistivity, and the red curve is the TTI parallel resistivity.

smaller and deeper in the parallel resistivity component of the TTI inversion, compared to the horizontal component of the VTI inversion, and appears to be more consistent with horizons picked from the seismic image.

Since a well has been drilled into the anticline structure, shown as a black vertical line in Figure 5, we have the possibility to compare the resistivity image from our VTI and TTI inversions to a resistivity log. Because the logging tool only measures the horizontal resistivity, we compare it to the horizontal/parallel resistivity component of the images. We upscale the well log measurements to a scale more appropriate for comparing to resistivity obtained from CSEM data by forming a moving harmonic average of the measured well log resistivity, with an averaging window of 200 m (Ellis et al., 2010). The upscaled well log resistivity compared to the VTI and TTI resistivity profiles is shown in Figure 7. We see that the parallel resistivity component from the TTI inversion provides a better match to the upscaled well log than the VTI inversion, especially in the shallow and deep parts of the well.

CONCLUSION

We have implemented TTI in 3D inversion of marine CSEM data, and applied our algorithm to both synthetic and field data. By comparing VTI and TTI inversion of our synthetic TTI model, we showed that imaging artifacts may appear in the VTI inversion, due to the inadequate description of the anisotropy. We also found that our TTI inversion was able to reconstruct the dip angles of the synthetic model starting from a simple isotropic halfspace, although more complicated models may require some prior information about the azimuth and dip angles to ensure convergence.

Applying our TTI inversion to a field data set acquired over a steeply dipping anticline, we found interesting differences between VTI and TTI inversions of the data. In particular, we found that a diffuse anomaly, seen in the VTI inversion in a syncline next to the anticline structure, was absent in the TTI inversion image. Finally, we found that the TTI inversion image provided a closer match to a well log from a borehole in the anticline structure, and had a better data fit.

ACKNOWLEDGMENTS

We thank TGS for permission to show the 2D seismic data from the Perdido fold belt, BOEM for permission to show the well log data, and EMGS for permission to publish the results.

REFERENCES

Davydycheva, S., V. Druskin, and T. Habashy, 2003, An efficient finite-difference scheme for electromagnetic logging in 3d anisotropic inhomogeneous media: Geophysics, **68**, 1525–1536.

Davydycheva, S., and M. A. Frenkel, 2013, The impact of 3d tilted resistivity anisotropy on marine csem measurements: The Leading Edge, **32**, 1374–1381.

Ellis, M., M. Sinha, and R. Parr, 2010, Role of fine-scale layering and grain alignment in the electrical anisotropy of marine sediments: First Break, **28**, 49–57.

Kanhalangsy, C., N. Golubev, J. J. Zach, and D. Baltar, 2011, Anisotropic csem inversion near the tiger well in ac 818, gulf of mexico: SEG Technical Program Expanded Abstracts, SEG, 609–613.

Li, Y., and S. Dai, 2011, Finite element modelling of marine controlled-source electromagnetic responses in two-dimensional dipping anisotropic conductivity structures: Geophysical Journal International, **185**, 622–636.

Lu, X., and C. Xia, 2007, Understanding anisotropy in marine csem data: SEG Technical Program Expanded Abstracts, SEG, 633–637.

Maaø, F. A., 2007, Fast finite-difference time-domain modeling for marine-subsurface electromagnetic problems: Geophysics, **72**, A19–A23.

Mohamad, S. A., L. Lorenz, L. T. Hoong, T. K. Wei, S. K. Chandola, N. Saadah, and F. Nazihah, 2010, A practical example why anisotropy matters a csem case study from south east asia: SEG Technical Program Expanded Abstracts, SEG, 696–700.

Morten, J. P., A. K. Bjørke, and A. K. Nguyen, 2010, Hydrocarbon reservoir thickness resolution in 3d csem anisotropic inversion: SEG Technical Program Expanded Abstracts, SEG, 599–603.

Morten, J. P., A. K. Bjørke, and T. Støren, 2009, Csem data uncertainty analysis for 3d inversion: SEG Technical Program Expanded Abstracts, SEG, 724–728.

Newman, G. A., M. Commer, and J. J. Carazzone, 2010, Imaging csem data in the presence of electrical anisotropy: Geophysics, **75**, F51–F61.

Zhu, C., R. H. Byrd, P. Lu, and J. Nocedal, 1997, Algorithm 778: L-bfgs-b: Fortran subroutines for large-scale bound-constrained optimization: ACM Transactions on Mathematical Software (TOMS), **23**, 550–560.